

Operation and performance of the NESTOR test detector

G. Aggouras^j, E. G. Anassontzis^{a,*}, A. E. Ball^d, G. Bourlis^f, W. Chinowsky^h, E. Fahrur^g, G. Grammatikakis^e, C. Green^g, P. Grieder^b, P. Katrivanosⁱ, P. Koske^g, A. Leisos^{i,f}, J. Ludvig^h, E. Markopoulos^j, P. Minkowsky^c, D. Nygren^h, K. Papageorgiou^j, G. Przybylski^h, L. K. Resvanis^{a,j}, I. Siotisⁱ, J. Sopher^h, T. Staveris^j, V. Tsagli^j, A. Tsirigotis^{j,f}, V. A. Zhukov^k

The NESTOR Collaboration

^a University of Athens, Physics Department, Greece.

^b University of Bern, Physikalisches Institut, Switzerland.

^c University of Bern, Institute for Theoretical Physics, Switzerland.

^d CERN (European Organization for Nuclear Research), Geneva, Switzerland.

^e University of Crete, Physics Department, Greece.

^f Hellenic Open University, School of Science and Technology, Patra, Greece.

^g University of Kiel, Institute of Experimental and Applied Physics, Germany.

^h Lawrence Berkeley National Laboratory, Berkeley, CA, USA.

ⁱ NCSR "Demokritos", Athens, Greece.

^j NESTOR Institute for Deep Sea Research, Technology and Neutrino Astroparticle Physics, Pylos, Greece.

^k Institute For Nuclear Research, Russian Academy of Sciences, Moscow, Russia.

Abstract

NESTOR is a deep-sea neutrino telescope that is under construction in the Ionian Sea off the coast of Greece at a depth of 4000 metres. This paper briefly reviews the detector structure and deployment techniques before describing in detail the calibration and engineering run of a test detector carried out in 2003. The detector was operated for more than one month and data was continuously transmitted to shore via an electro-optical cable laid on the sea floor. The performance of the detector is discussed and analysis of the data obtained shows that the measured cosmic ray muon flux is in good agreement with previous measurements and with phenomenological models.

NESTOR NEUTRINO TELESCOPE DEEP-SEA PERFORMANCE

* Corresponding author:

Ass.Prof. E.G. Anassontzis

University of Athens, Faculty of Physics

Nuclear and Particle Physics Dep.

Panepistimioupolis

15771 Ilisia, Athens

Greece

eanason@cc.uoa.gr

1. Introduction

When high-energy neutrinos interact with matter they produce relativistic muons that follow closely the direction of the incident neutrinos. When such interactions occur in the sea water or bedrock close to the detector, these muons can be observed by the Cherenkov light that they emit using arrays of sensitive optical detectors: from the arrival time and intensity of the light pulses detected, the direction of the muons, and hence those of the incident neutrinos, can be reconstructed.

The potential of such detectors for astronomy and cosmology has long been recognised. After the pioneering work by DUMAND [1] near Hawaii, detectors are currently operating at Lake Baikal (Siberia) [2] and in ice at the South Pole (AMANDA) [3]. Construction of a large array (ICECUBE [4]) is starting at the South Pole and the need for a complementary detector ($\sim 1 \text{ km}^3$) in the northern hemisphere has led to a number of projects in the Mediterranean [5, 6, 7].

2. Main features of the NESTOR Detector, its site and infrastructure

A number of reports and papers have described in detail the elements of the NESTOR detector and the techniques used for its deployment and recovery [8-13]. The main features are only briefly reviewed in this section.

The prerequisites for the site are deep (many km), clear water, low underwater currents, very low bioluminescent activity, minimal sedimentation and biofouling rates as well as close proximity to support infrastructure on shore. The NESTOR site in the Ionian Sea off the southwestern tip of the Peloponnese fulfils all these requirements. Extensive surveys in 1989, 1991 & 1992 [14, 15] located a large flat plateau of $8 \times 9 \text{ km}^2$ in area at a mean depth of 4000 metres. Situated on the side of the Hellenic Trench that lies between the west coast of the Peloponnese and the submarine mountain chain of the East Mediterranean Ridge, the site is well protected from major deep-water perturbations. The deepest water in the Mediterranean at 5200 metres is a few miles from the NESTOR site. Very deep water is essential in reducing the principal background from muons produced by cosmic rays interacting in the Earth's atmosphere: biological activity also diminishes with depth.

The location¹ is 7.5 nautical miles from the island of Sapienza, where there are two small harbours, and 11 miles from the port of Methoni: substantial port facilities are available 15 miles away in the town of Pylos on the bay of Navarino.

Regular measurements [16, 17] of water quality show transmission lengths of $55 \pm 10 \text{ m}$ at a wavelength of 460 nm, stable temperatures of 14.2°C and water current velocities well below 10 cm/s [18]: light bursts of 1-10 s duration, consistent with bioluminescent activity, represent around 1% of the active time and there is little/no evidence of problems due to sedimentation or bio-fouling [19]. The sea bottom over the site has a clay deposit accumulated over some tens of thousands of years which provides for good anchoring.

¹ Site coordinates: $36^\circ 37.5' \text{ N}$, $21^\circ 34.6' \text{ E}$

A shore station has been established in Methoni where the land end of the 30 km long electro-optical cable is terminated. The main d-c power converter for the electrical supply, the monitoring and control systems and the land end of the data acquisition system are located in the Methoni building.

The basic element of the NESTOR detector is a hexagonal floor or star. Six arms, built from titanium tubes to form a lightweight lattice girder, are attached to a central casing: two optical modules are attached at the end of each of the arms, one facing upwards and the other downwards. The electronics for the floor is housed in a one-meter diameter titanium sphere within the central casing. The nominal floor diameter at the optical modules is 32 metres.

A full NESTOR tower would consist of 12 such floors stacked vertically with a spacing of 30 m between floors. This is tethered to a sea bottom unit (pyramid) that contains the anchor, the junction box, several environmental sensors and the sea electrode that provides the electrical power return path to shore: the junction box houses the termination of the sea-end of the electro-optical cable, the fan-outs for optical fibres and power to the floors etc. as well as monitoring and protection of the electrical system.

The optical module [20] consists of a 15" diameter photomultiplier tube (PMT) enclosed in a spherical glass housing which can withstand the hydrostatic pressure up to 630 atmospheres. To reduce the effect of the terrestrial magnetic field, the PMT is surrounded by a high magnetic permeability cage [21]. Optical coupling of the PMT to the glass sphere is made with glycerine, sealed by a transparent silicon gel gasket. The high voltage for each PMT is generated by a DC-DC converter within the glass sphere: the PMT signal, 24 V power, control and monitoring signals are connected through a single 7-pin connector and hybrid cable to the central titanium sphere with the floor electronics.

Other modules, above and below each floor, house LED flasher units that are used for calibration of the detector: these are controlled and triggered from the floor electronics.

Deployed [13] equipment is brought to the surface, together with the sea end of the electro-optical cable, by means of a recovery rope, released from the sea bottom by an acoustic signal. Modifications or additions to the experimental package are made at the surface and all connections are made in the air with dry-mating connectors. The cable and experiment systems are then re-deployed and the recovery rope, with its acoustic release laid on the seabed.

The NESTOR deployment 'philosophy' has always been to avoid the need for specialised manned or unmanned underwater vehicles for deployment and recovery operations that require the use of manipulators, wet-mating connectors and consequent high costs. All electrical and optical fiber connections are dry mated in the air.

The objectives for the deployment reported in this paper were to test fully the electrical supply and distribution systems, the monitoring and control systems and the full data acquisition and transmission chain from the sea to the shore station.

The electro-optical cable and the sea bottom pyramid, which had been deployed in previous operations, were brought to the surface. A detector star with 12 optical modules was attached, cabled to the junction box and redeployed to 3800 metres.

The titanium girder arms of the stars are made in standard modules of 5-meter length: for logistical reasons on the deployment vessel, the star used for this experiment has an overall diameter of 12 metres. In all other respects standard equipment was used. The detector star is located 80 metres above the sea bottom pyramid. The system was

powered and monitored during deployment: the PMTs were switched a few hours later when they had reached a quiescent state after brief exposure to daylight.

The system was operated continuously for more than a month and several million events recorded. This has not only provided invaluable experience on the operation of the detector but has initiated the development and testing of powerful tools for reconstruction and analysis.

3. Readout, Control and Data Acquisition systems

In the Ti-sphere, the electronics is divided into two main units, the Housekeeping Board that handles the system monitoring and control functions, and the Floor Board that handles signal treatment and communications. The two boards, connected by flat cable, are mounted on an aluminum sub-frame that also carries the local sensors and dc-dc converters. All connections from outside of the sphere are routed via patch panels on the sub-frame so that the complete unit can be removed and fully tested in the laboratory or connected through the ‘sea’ connectors in the Ti-sphere. The sub-frame is electrically isolated from the sphere.

In the Shore Station counting room, all communication with the deployed detector floor are handled by a single electronics board, the Shore Board [22,23] that sits on the EISA bus of the main server in the Data Acquisition (DAQ) computer cluster. Connection between the Shore and Floor Board is via two monomode optical fibres in the electro-optical cable.

The Shore Board receives the data packages via the ‘up-link’, which are stored temporarily in local buffers. It broadcasts a global 40MHz clock signal via the ‘down-link’ to the Floor Board, sends commands to set the run or calibration parameters and initiates functions to be executed by the Housekeeping board. The ‘down-link’ can also be used to re-program the FPGA/PLDs within the Floor Board and change the trigger logic parameters.

The Housekeeping Board [24] controls the distribution of power to the PMTs as well as setting and monitoring the PMT’s high voltage supply that is generated within the optical modules. The board also records information from the environmental sensors (compass and tilt meters, thermometers, humidity and hygrometry) inside the Ti-sphere and from other sensors (e.g. water pressure and flow meters) that can be mounted externally. The Housekeeping Board also operates the LED flasher units of the calibration system.

The Floor Board handles the PMT signal sensing, majority logic event triggering, waveform capture, digitization and event formatting [23,24]. It also handles the communications with the shore board, the ‘up-link’ sending the data to shore and the ‘down-link’ receiving the clock signal, commands and downloads of operational parameters.

The heart of the DAQ system is a novel ASIC developed at LBNL, the “Analog Transient Waveform Digitizer” (ATWD) [25]. Each ATWD has four channels with 128 common-ramp, 10-bit, Wilkinson ADCs that, after activation, digitize all 128 samples of a selected channel. An active delay line generates the sampling so that no clocks are involved in waveform capture. The sampling rate is determined by a single external current and may be varied from 200M samples/s to 2G samples/s.

A sampling speed of 273M samples/s was selected in order to capture the PMT signals and to recognize overlapping pulses, giving a sampling period of 3.66ns. This gives a

dynamical range (active time window) for each ATWD channel of 465ns. There are five ATWDs on the Floor Board, providing twenty digitization channels. Twelve are used to digitize the PMT waveforms whilst five channels (one per ATWD) are used to digitize the waveform of the 40MHz clock signal, broadcast from the shore board: this gives a continuous check of the sampling interval stability. A further channel is used to digitize the trigger majority logic signal to provide information for the synchronization and timing checks. The last two channels are used for internal calibration functions. A further feature of the floor board is a standard pulse generator: in calibration mode, the pulse can be applied to all ATWD 'data' channels and digitized to continuously calibrate the gain of each channel.

An event selection trigger is generated when the majority coincidence requirement between PMT signals above a certain threshold level (typically 30mV), is satisfied. The trigger window is adjustable to cover different maximum distances between the optical modules. With the physical layout of the detector floor presently deployed, the trigger window was set at 60ns.

The leading edge of the majority logic signal (corresponding to the time when the last of the PMT pulses participating in the trigger crosses the threshold level) is used to define the absolute time² of the trigger occurrence with respect to the 40MHz clock. The occurrence of the trigger initiates waveform capture by the ATWDs, reading of the environmental parameters and data transmission to the shore. The relative delays between the electronics cause the event trigger to occur at 197.5 ns within the active time window.

It is also possible to generate a forced trigger by command from the shore control system that initiates digitization and data transmission. This test function is especially useful for taking data during the deployment operations when the PMTs are not powered.

The sampling period, as well as the gains of the ATWD channels have been continuously monitored and found extremely stable during long time periods. Figure 1 shows the stability of the ATWD sampling during a long data-taking run. Each entry to the histogram is an estimated value of the sampling interval, using the digitized waveforms of the 40MHz clock in an event. The standard deviation of this distribution is 5ps, which is negligible compared to the mean value of the sampling interval of 3.66ns.

² This timestamp characterizes the time of occurrence of a floor event. It is transmitted to the shore inside the data package and in a future multi-floor NESTOR detector will be used to build a global event by combining experimental information from several floors.

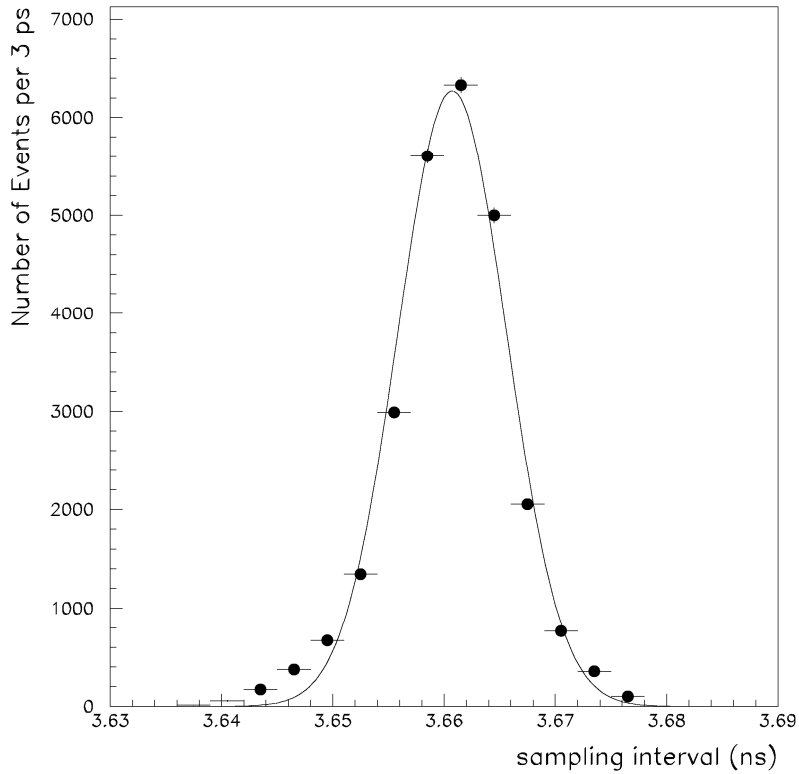


Figure 1: Distribution of the sampling intervals of an ATWD estimated on an event-by-event basis, during data taking. The curve corresponds to a Gaussian function of mean value and sigma equal to 3.66ns and 5ps respectively.

The Data Acquisition (DAQ) computer cluster at the shore laboratory consists of three distinct subsystems, the Server, the Fast Monitor and the Data Quality Checking subsystem, performing the following complementary tasks:

(i) The Server subsystem controls, through the Shore Board, the experimental parameters, the main functions of the DAQ and receives the data streams. After a fast structural check of the data packages, it builds event files and manages the recording on the storage media (hard discs and CD-ROMs). In parallel, it provides sample event files to the Fast Monitor subsystem. These are groups of thirteen consecutive events picked up uniformly in time from the data stream. The period of this event sample selection can be adjusted according to the needs of the run. A typical selection period, when the experiment runs with a trigger rate of about 4Hz is of the order of 10sec. This subsystem is also responsible for the construction and updating of a database (electronic logbook) containing detailed information about the DAQ status, as well as the summary of the experimental parameters and the environmental conditions relative to each data file.

(ii) The Fast Monitor subsystem runs an interactive software package, developed in LabView. This package uses the sample event files provided by the Server subsystem, performs fast analysis operations, builds parameter files and histograms within an interactive, graphic display environment.

The environmental conditions of the detector are continuously monitored, such as the floor orientation (compass and tilt meters), the temperatures, humidity and hygrometry within the titanium sphere, the external water temperature and pressure and data from

other environmental instruments mounted on the sea bottom station (pyramid). In addition, the electrical power distribution network and the high voltages applied to the PMTs, the PMT counting rates, the trigger rates, majority logic rates as well as other parameters relative to DAQ performance (dead time, number of corrupted events etc.) are also monitored continuously.

An alarm network within the Fast Monitor subsystem is activated when any of the monitored parameters deviates beyond the predefined tolerance values. The Fast Monitor also builds summary files on demand and records information in the electronic logbook. The event display feature gives the operator an opportunity to quickly check the PMT waveform digitization, during data taking.

(iii) The Data Quality Checking subsystem performs a fast reconstruction analysis on small subsets of the accumulated events during data taking to check the integrity of the data and ensure that the selection trigger is unbiased. It complements the Fast Monitor by performing detailed signal processing (as described in Section 4) and provides additional information on the performance of the PMTs, the triggering, digitization and readout electronics. This includes the stability³ of, the PMT pulse height distributions, the ATWD gain and sampling interval, the majority coincidence rate and the distribution of the total number of photoelectrons inside the trigger window. Furthermore, it checks the trigger formation and timing with respect to the digitized PMT pulses and the dependence of the total number of accumulated photoelectrons inside the coincidence window⁴ to the coincidence level. The subsystem provides a fast track, 'on-line' reconstruction on the hypothesis that the data corresponds to muons passing through the fiducial volume of the detector.

4. Detector Calibration and Signal Processing

Each of the 128 Wilkinson ADCs of an ATWD has its own pedestal. This has to be subtracted from the digitized PMT waveform, on a sample-by-sample basis, in order to bring the base line to zero. The measurement of the pedestals was made in the laboratory before the deployment. The stability of the pedestals was checked⁵ using the accumulated data during the 2003 run and was found to remain constant with variations of less than 1% over time.

The propagation of the PMT signals through the transmission lines to the ATWDs causes amplitude attenuation and broadening of the pulse shape. This is mainly due to the delay lines just before the pulse reaches the ATWDs (AV1258, time delay $t_d=250\text{ns}$, $Z=750\Omega$, rise time $r_t=12\text{ns}$). In order to reconstruct the original PMT pulse properties, the digitized waveforms must be corrected. Each individual PMT transmission line, including the cable from the PMT to the Floor Board and all corresponding passive and active electronic elements up to the ATWD, has been calibrated and the signal attenuation measured in the laboratory before deployment of the detector.

A very narrow electronic pulse was propagated through each PMT transmission line and digitized at the corresponding ATWD channel. The Fourier spectra of the input pulse and the digitized waveform (after pedestal subtraction) were compared to produce a signal

³ Under constant event selection criteria.

⁴ This is the sum of the PMT pulse heights (in units of the mean value of the one-photoelectron pulse height distribution) inside the coincidence window

⁵ When collecting data with a 4-fold coincidence trigger, the majority of the events contain 8 empty ATWD channels.

attenuation correction as a function of frequency, the ‘so-called’ response function. Figure 2 shows the amplitude and phase of the response function for a typical transmission line. It has been verified in the laboratory that, by applying these corrections to the digitized PMT pulses, the original shape and amplitude characteristics of the pulses are recovered.

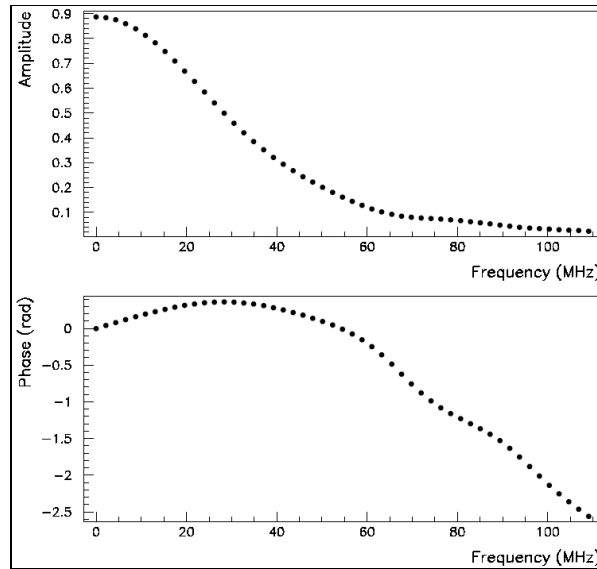


Figure 2: The amplitude and phase of the response function of a PMT transmission line.

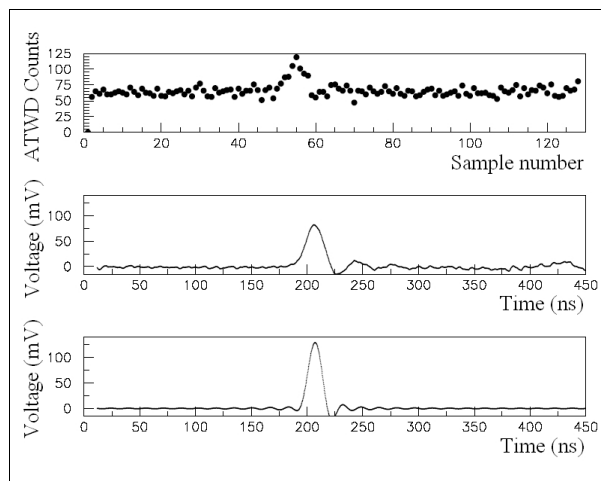


Figure 3: Demonstration of the signal processing stages. Top: The raw digitized waveform. Middle: The waveform after pedestal subtraction, sample number to time and ATWD count to voltage conversion. Bottom: The recovered waveform after the attenuation correction.

Figure 3 gives an example of the first two stages of standard processing of the digitized waveforms. First, the pedestals are subtracted on a sample-by-sample basis. Extra points, between the 128 original samples of the digitized waveform are estimated by means of a quadratic interpolation. The coordinates are transformed to voltage (mV) and time (ns), using the known ATWD gains and sampling intervals respectively. Then the waveform undergoes a discrete Fourier transformation. The Fourier coefficients are modified using the corresponding attenuation corrections. The corrected waveform is recovered by means of an inverse Fourier transformation.

The PMT pulse arrival time is defined after this stage, as the time where the tangential to the rising edge of the pulse shape at the inflection point intersects with the base line. This definition is found to be the least dependent on the pulse amplitude (slewing). Note that for some checks and comparisons with the hardware trigger, the arrival time is taken to be the time when the rising edge of the PMT pulse crosses a threshold level (typically 30 mV).

Figure 4 shows the effect of the two first processing stages on a single PMT pulse. The rise time of 14ns of the raw PMT digitized pulse is transformed to 8ns after signal processing: this is in a very good agreement with the measured characteristics of the PMTs. This correction has an important effect on the estimation of arrival time of the PMT pulse and consequently on the tracking accuracy (e.g. muon direction resolution) of the detector.

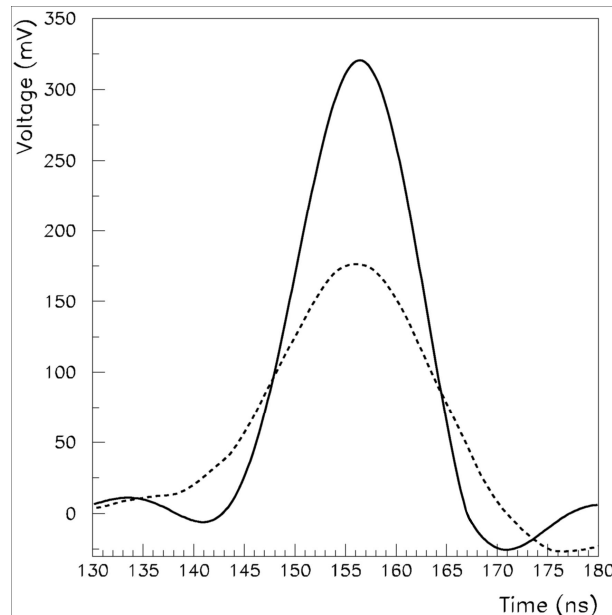


Figure 4: A PMT pulse before (dashed line) and after (solid line) the attenuation correction.

Figure 5, shows the distribution of the time differences between the hardware and software trigger signals, before and after signal processing, for events collected at the experimental site. The trigger selection signal is latched in one of the ATWD channels, whilst the software trigger is reconstructed by applying the same trigger logic to the digitized PMT pulses. After the attenuation correction, the accuracy of the PMT arrival time is fully recovered, resulting in the reconstruction of the trigger timing to 0.8 ns.

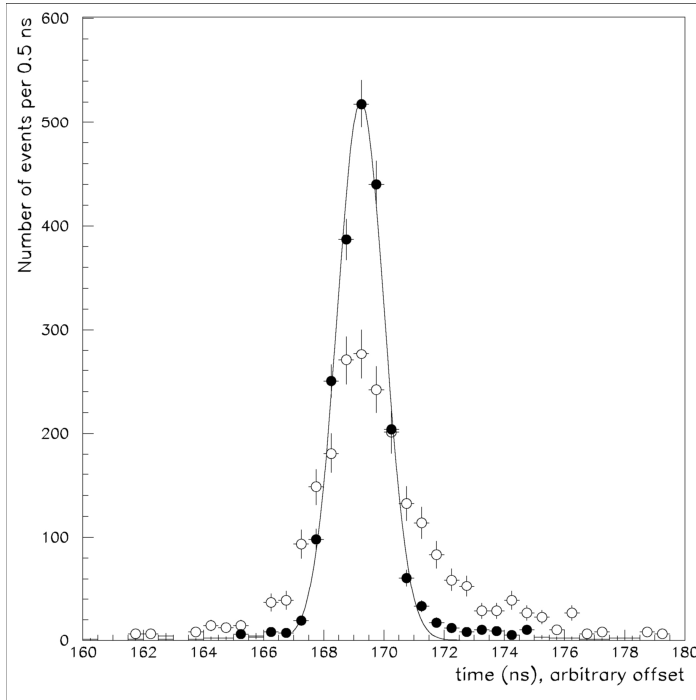


Figure 5: The distribution of the time differences between the hardware and software trigger, before (open circles) and after (solid points) signal processing. The solid line represents a Gaussian fit to the time difference with a sigma of 0.8ns.

There are cases where the digitized waveform of the PMT includes overlapping pulses. In many such cases, the overlap can be disentangled after the two first steps of the signal processing. This is demonstrated in Figure 6 where the standard correction of the original pulse shape results in the resolution of the two overlapping pulses.

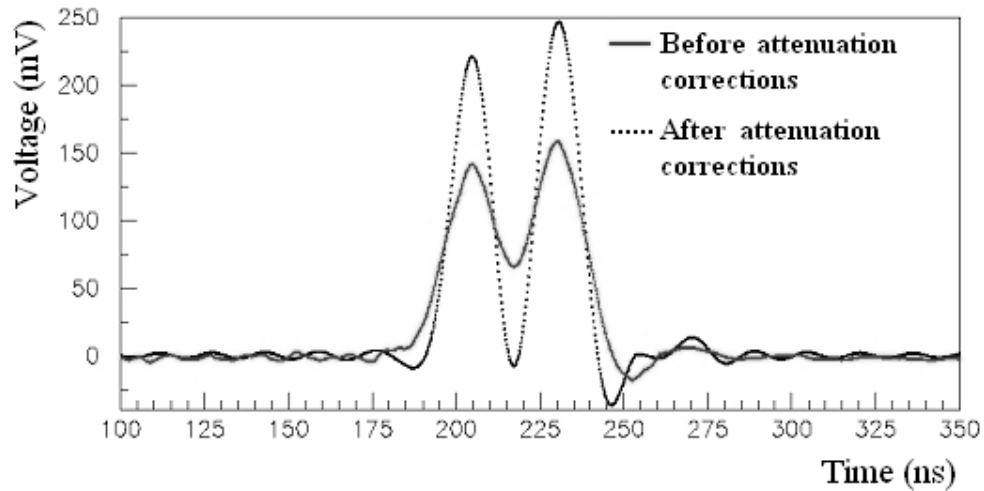


Figure 6: Separation of overlapping pulses after the attenuation correction.

However, there are some cases where the overlapping is not resolved at this stage. These pulses can often be separated in a third processing stage by a χ^2 fitting using standard pulse shapes. An example of such a fit is shown in Figure 7.

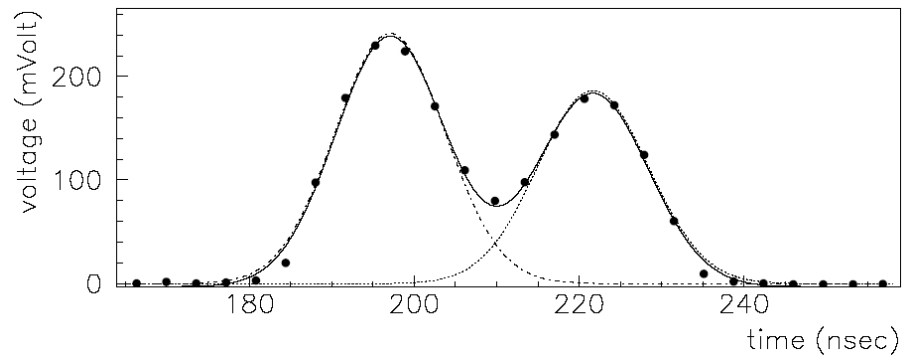


Figure 7: Separation of overlapping pulses by means of a χ^2 fit.

Finally, PMT pulses of very high amplitude, which exceed 1.8Volts (more than 15 photoelectrons), cause overflows in the digitization electronics. These pulses undergo an extra pre-processing, before the attenuation correction, that includes pulse shape fitting and amplitude estimation.

The twelve optical modules used in the present deployment (and a number of spares) have been simultaneously illuminated in the laboratory using the calibration LED flasher unit. The full data acquisition and analysis chain was used and the LED was operated at several levels of light output. The collected calibration data has been used to optimize the working point (PMT high voltage), synchronize the PMT pulse arrival times and measure

the characteristics of the PMT pulse height distribution, corresponding to the emission of one photoelectron from the photocathode⁶.

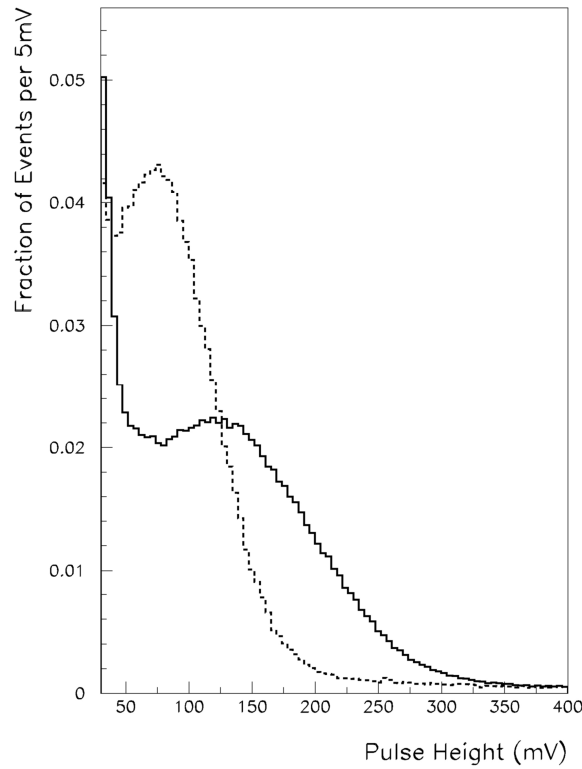


Figure 8: PMT pulse height distribution due to K^{40} background before (dashed line) and after (solid line) the signal processing.

Figure 8 demonstrates the effect of the signal processing on the digitized PMT pulse amplitude from the deployed detector. It shows the pulse height distribution of a PMT before and after the processing stages described above. The data presented have been selected with a 4-fold or higher-level coincidence trigger during normal data taking at the experimental site. The majority of these events are due to random coincidences of pulses from K^{40} decays. The emitted electrons produce Cherenkov light at the level of a few photoelectrons. The corrected pulse height distribution is in a very good agreement with the results of the calibration data accumulated in the laboratory before the deployment of the detector (see Section 6).

5. Detector Simulation

We have developed a simulation package that describes in detail the detector architecture and its functionality, as well as the physical processes related to an underwater neutrino telescope. It was extensively used for studying the overall

⁶ It will be referred to as “one photoelectron pulse height distribution” hereafter. The mean values of these distributions, for the selected operating values of the PMTs high voltages, were about 120 mVs.

performance of the detector and data analysis. The simulation process consists of two phases. In the first phase, we simulate the physical processes resulting in the production of Cherenkov photons and the propagation of the photons through the water and the materials surrounding the PMT [20] until they arrive at the photo-cathode. In the second phase we simulate in detail the PMT response, the functions of the electronics and the data acquisition system.

In the first simulation phase, all known processes that can occur when a neutrino interacts or when a charged lepton passes through the matter surrounding the detector are included. Since the signal is produced by the Cherenkov photons that hit the photocathode of the PMTs, special attention is given to the Cherenkov radiation and the propagation of light in the water and through the Optical Module. The tool used in this stage is the GEANT 4 simulation package [26] and its interfaces with other packages such as Pythia, EGS etc. All the energy losses of the particles involved (ionization, atomic excitation, bremsstrahlung, pair production, muon-nucleus interaction, formation of electromagnetic and hadronic showers etc.) as well as multiple scattering are taken into account. The simulation package tracks every primary and secondary particle between consecutive interactions. At each step Cherenkov photons are generated, which may interact either by absorption, or by scattering in the water, before they reach the Optical Module. The Optical Module [20] consists of many components, which are described in detail in the simulation. For this we used a geometrical description of the benthos sphere (the glass housing of the PMT), the glycerin (the optical coupling between the glass envelope and the PMT) and the shading caused by the magnetic shielding cage. The optical properties of each component, such as the absorption length and the refractive index, are taken as a function of the photon wavelength.

The second phase includes the generation of single electrical pulses, the contribution of the background sources, the generation of the PMT waveforms and the functions of the electronics. The simulation in this phase is based on the following assumptions:

- a) The emission of photoelectrons is a stochastic process. Each photon of a certain wavelength (λ) liberates an electron from the photocathode (photoelectrons) according to a Poisson distribution. The mean of the Poissonian is the product of the quantum efficiency of the photocathode at wavelength λ and the collection efficiency, which depends on the position where the photon hits the photocathode [20].
- b) Each emitted photoelectron produces a single electrical pulse at the anode with an amplitude that follows the one photoelectron PMT pulse height distribution: this has been measured in the laboratory for each individual PMT.
- c) The functional form, which describes the electrical pulse shape, was defined by fitting digitized PMT pulses measured in the laboratory.
- d) The transition time of the PMT pulses varies according to a Gaussian distribution measured for each PMT separately [20].
- e) The PMT response to 'n' photoelectrons is a linear sum of the pulses simulated for each individual photoelectron.
- f) Background pulses due to thermionic noise and the after and late pulses of the PMT are added to each event. The characteristics of the first contribution (the pulse height distribution, and counting rate) have been measured in situ (see section 6) whilst the emission of after and late pulses has been studied extensively in the laboratory [20].

g) K^{40} radioactivity in the water produces an optical background that has been extensively studied at the deployment site (see section 6). The corresponding measured electrical counting rate and pulse height distribution are used to add this background noise in the simulation of each PMT signal.

h) The final PMT waveform generated is the linear sum of all the signal and background pulses.

The generated PMT waveform then follows a simulated electronics data chain to include i) the pulse attenuation and propagation through the signal transmission line, ii) the trigger formation and iii) the digitization of the pulses.

As a final step in the procedure, the simulated events are formatted using the same data protocol as the Data Acquisition System. In this way Monte Carlo generated events have the same format as the experimental data and can be analyzed with the same tools.

The Monte Carlo package has been used to produce event samples of simulated detector response to background sources only and to atmospheric muons⁷ arriving at the detector depth. A large number of muons ($2.26 \cdot 10^7$) have been generated within a circle of 100m radius, 100m above the detector, with energy and angular distributions taken from the phenomenological parameterisation of Okada [27].

6. Detector Performance

The deployed detector was operated continuously for more than a month and over five million events were accumulated, investigating different trigger modes, coincidence levels and PMT thresholds. In addition, several million calibration events were taken at various PMT high voltage levels or using the LED flash units. Of this total data, some two million events were accumulated under constant running conditions with a 4-fold or higher coincidence trigger and 30mV PMT threshold: this event sample has been used for the following performance analysis and for track reconstruction.

The readout and DAQ chain was operated continuously with practically no dead time and the monitored experimental parameters (environmental and operational) remained stable within tolerances. The PMT counting rates remained stable during the whole running period at a level of around 50kHz per PMT, due principally to Cherenkov light emitted by electrons from K^{40} decays. The PMT counting rate (inside the 60ns window) was found to remain constant as a function of the coincidence level, showing that the trigger is not biased by the rate.

A majority of the events, accumulated with a 4-fold coincidence trigger, result from accidental coincidences between PMT pulses from the K^{40} background. Consequently, the PMT pulse height distribution shape should remain stable, corresponding to the emission of a very few photoelectrons

In a typical example shown in Figure 9, the pulse height distribution has a shape corresponding to a few (average 1.3) photoelectrons. This distribution can be described very well as the overlay of the one-photoelectron (see insert plot) and two-photoelectron pulse height distributions, measured in the laboratory during the detector calibration.

⁷ The Monte Carlo muon event samples contain also contribution from background sources.

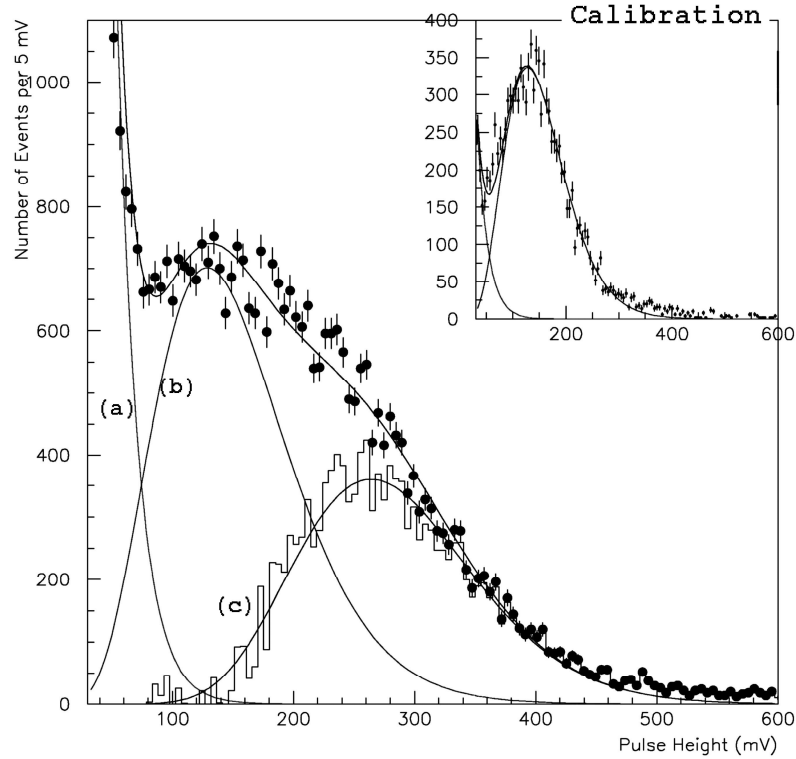


Figure 9: The pulse height distribution of a PMT during operation in deep sea (main plot) and from a calibration run in the laboratory (insert plot). The solid line in the main plot is the result of a fit to the data points using an exponential shape for the dark current (line a), as well as the one photoelectron (line b) and the two photoelectrons (line c) pulse height spectra evaluated during calibration runs at the laboratory.

The K^{40} background has been used as a stable ‘standard candle’ in order to monitor the gain stability of the detector. The PMT pulse height distributions from each data file were compared to a standard shape defined at the beginning of the run and found to be extremely stable for all of the PMTs during the whole running period.

However, there were periods of time when the instantaneous counting rates of a group of PMTs and the collection trigger rate show a large increase: Figure 10 gives an example of such behavior. The downlooking group of PMTs exhibits a synchronous increase of counting rates whilst the others remain relatively quiet, indicating that there is probably a localized light source below the detector. These phenomena last typically from 1 to 10sec and represent a total 1.1% of the active experimental time. The effect is consistent with bioluminescent activity from microorganisms around the detector.

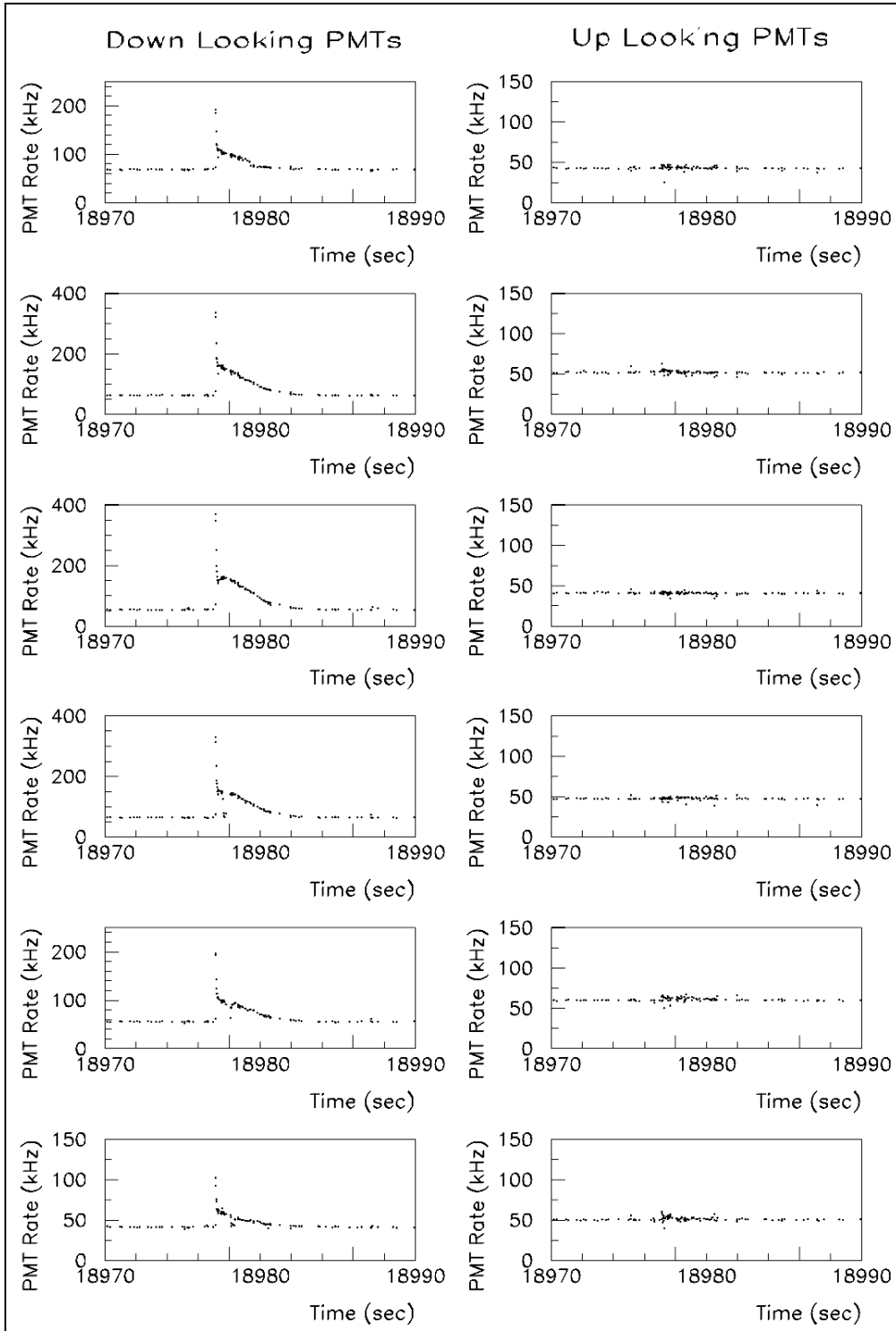


Figure 10: PMT counting rates as a function of time during bioluminescent activity. Each row represents a pair of PMTs on the same arm of the hexagonal detector floor.

The pulse height distribution of the PMTs during a period of bioluminescence is very similar to the distribution due to the K^{40} decay. To demonstrate this, Figure 11 compares

the distribution of the total number of accumulated photoelectrons inside the trigger window with a 4-fold or higher level coincidence trigger for events collected during periods with and without bioluminescence activity.

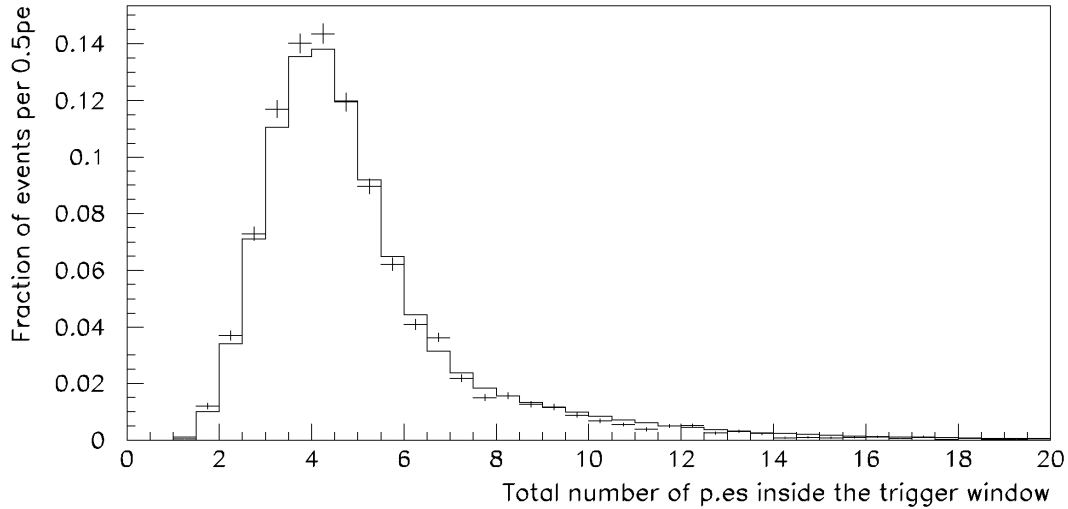


Figure 11: The total number of accumulated photoelectrons inside the trigger window during bioluminescence activity (crosses) and with no bioluminescence (histogram).

Bioluminescence can be easily identified because of its characteristic time duration and therefore does not cause any background problem. In the following analysis, all events collected during periods of bioluminescence activity have been excluded: this represents a reduction of only 1.1% in the size of the data sample⁸.

The average experimental trigger rate, corresponding to the coincidence of four or more PMT pulses above 30mV amplitude, was 3.76Hz compared to an estimated rate of 3.79Hz derived from the Monte Carlo simulations (see section 5).

According to the Monte Carlo estimation, only a small fraction (5.5%, 0.21Hz) of this trigger rate corresponds to atmospheric muons passing close to the detector. When the PMT thresholds were set to 120mV, the measured trigger rate was 0.29Hz, in agreement with the equivalent Monte Carlo estimate of 0.30Hz.

Furthermore, the measured coincidence rates, shown in Figure 12, are in very good agreement with the Monte Carlo estimations for several levels of coincidence at different PMT thresholds. In the same plots, we present the Monte Carlo estimated contribution of the atmospheric muon flux to the triggers, showing that higher-level coincidences exclude the combinatorial background. A better rejection of the combinatorial background is achieved at higher PMT threshold values.

⁸ High levels of bioluminescence can cause severe dead-time in data taking at some sites [28].

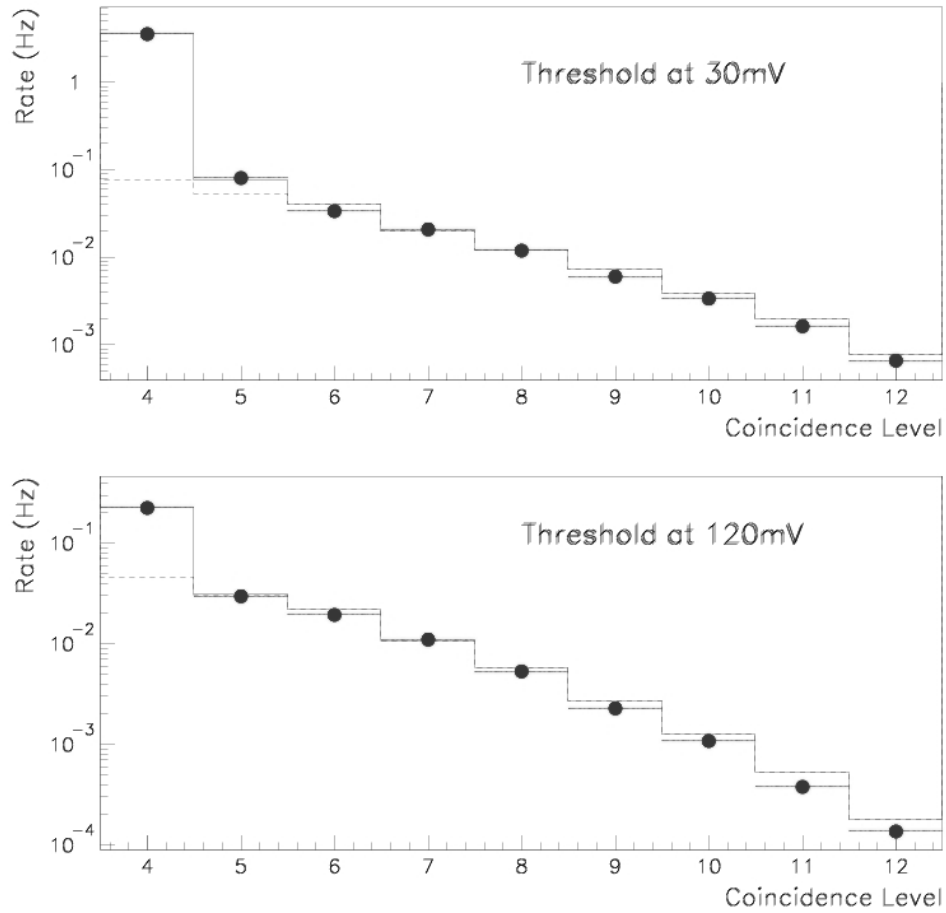


Figure 12: Trigger rates as a function of the coincidence level, for two threshold settings. The points represent the data, the solid line the Monte Carlo estimation including background and the dashed line the Monte Carlo estimation for the contribution of the atmospheric muons.

Several studies have been made to ensure that all the collected light on the PMTs can be attributed to the known sources. Since higher coincidence levels reject better the combinatorial background, the dependence of the total number of collected photons per event on the coincidence level has been studied. The total number of accumulated photoelectrons inside the coincidence window has been used as a measure of the total number of collected photons. The mean value of the number of accumulated photoelectrons inside the coincidence window, as a function of the coincidence level is compared to the Monte Carlo prediction in Figure 13. As expected, there is a faster than a linear increase with respect to the multiplicity of the coincidence, in very good agreement with the Monte Carlo prediction.

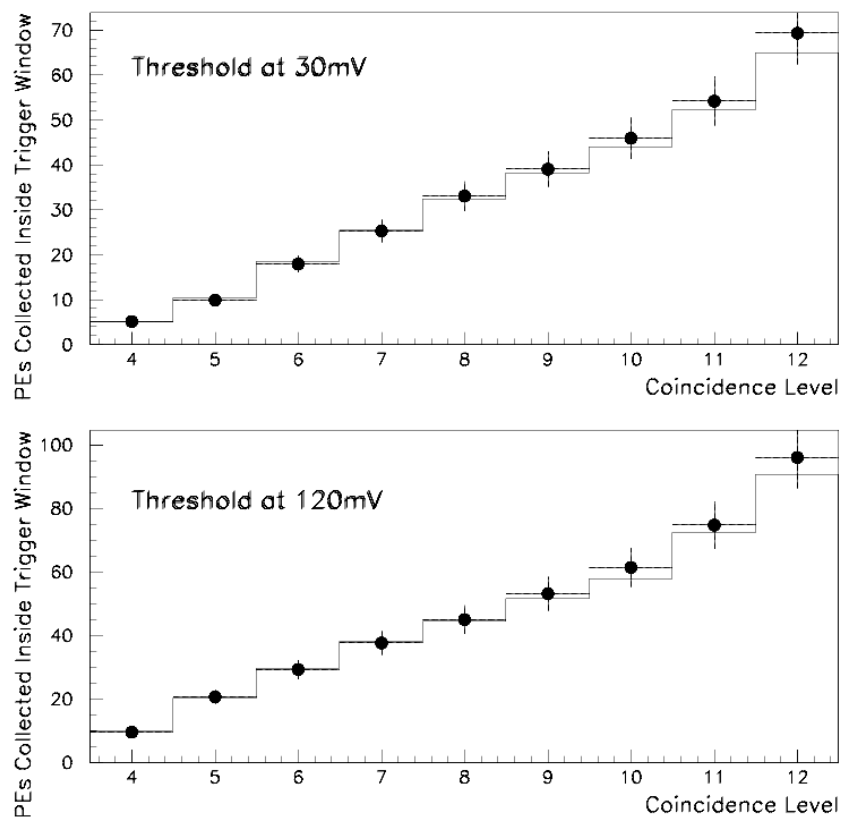


Figure 13: Total number of photoelectrons inside the coincidence window as a function of the coincidence level for two threshold settings. The points represent the data and the histogram gives the Monte Carlo estimation.

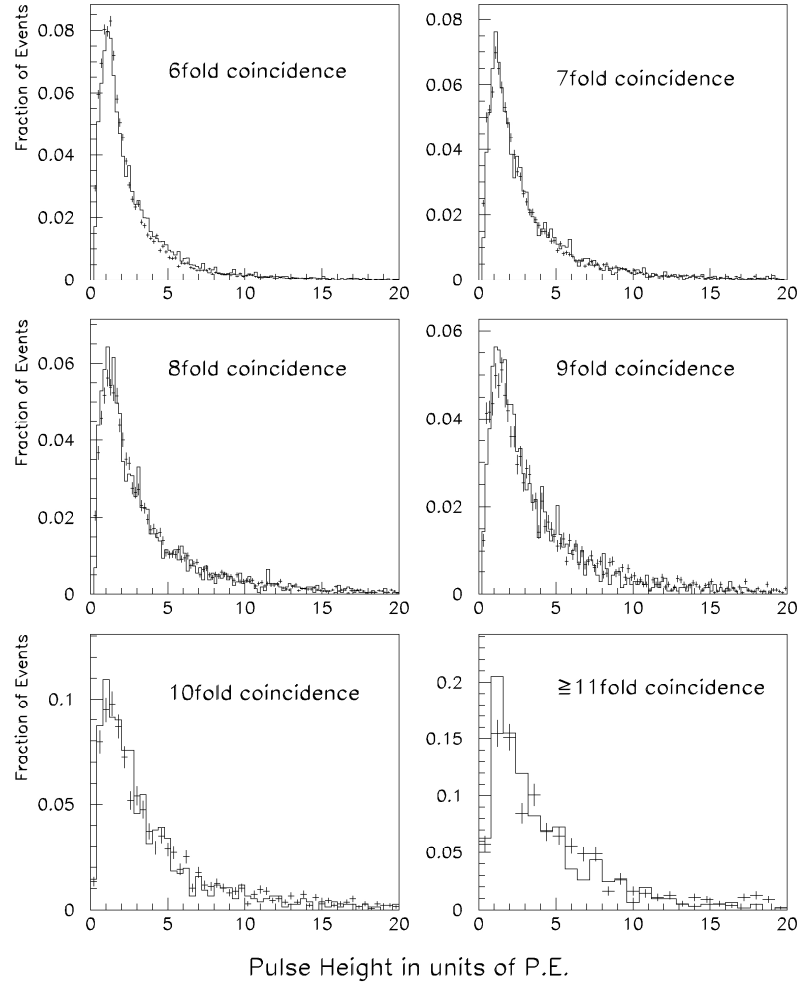


Figure 14: The pulse height distribution of a typical PMT, in units of the mean value of the one photoelectron distribution, participating in a high level coincidence. The crosses represent the data whilst the histograms show the corresponding Monte-Carlo prediction.

Another sensitive test is to examine the pulse height distributions of individual PMT pulses that contribute to events with high multiplicity coincidences: these are typically pulses produced by atmospheric muons. The pulse height distribution of a typical PMT (in units of the mean value of the one photoelectron spectrum), when participating in a 6-fold or higher coincidence, is shown in Figure 14 and is compared to the Monte Carlo estimation. The agreement between the measured and predicted spectra, which has been verified for all PMTs of the detector, indicates that the collected light is produced by the sources that are used in the detector simulation

Finally, the global arrival time distribution of the accumulated photoelectrons was studied, for events with at least six PMT pulses inside the coincidence window. This is the distribution of the arrival time of any digitized PMT pulse, weighted by the pulse amplitude (in units of the mean value of the one photoelectron pulse height distribution) and normalized to the total number of selected events. This distribution expresses the correlation of the Cherenkov light intensity and the arrival time. As shown in Figure 15, the Monte Carlo simulation agrees, within statistical errors, with the experimental global arrival time distribution of the accumulated photoelectrons.

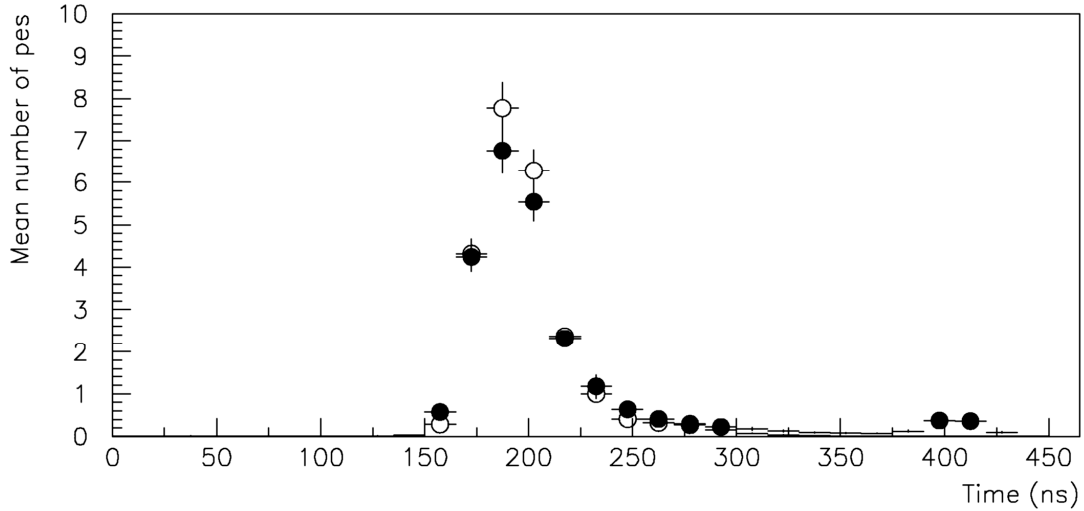


Figure 15: Global arrival time distribution of the accumulated photoelectrons (solid points) compared with the Monte Carlo expectation (open circles) for events with six or more PMT pulses inside the trigger window.

At the end of the active experimental window there is a small peak in the data that does not appear in the Monte Carlo expectation. This is due to a known malfunction in the first generation of ATWDs, which digitize a low amplitude ghost pulse at the end of their active window. This problem does not affect the analysis because only pulses inside the trigger window are used.

Data from calibration runs with the LED flasher units was used to monitor operation at the deep-sea site. In particular, this data has been used to check the detector time resolution.

The PMTs are positioned symmetrically with respect to the LED flasher unit so the digitized PMT pulses are expected to have the same arrival time, within measurement errors. The distributions of the arrival time difference between pulses of any pair of PMTs, produced by the same LED flash and with a pulse height greater than 800mV, show a peak at zero time with a standard deviation compatible to the light pulse duration convoluted with the arrival time resolution. However, when we choose the pulses of the first PMT to have lower amplitude, the mean difference of the arrival times deviates from zero and the standard deviation of the distribution increases. The first effect is a result of the dependence of the arrival time definition on the pulse amplitude (slewing), whilst the second effect reflects the transient time spread [20] and the pulse reconstruction resolution dependence on the amplitude of the pulse. These dependencies are measured using the calibration data and parameterised in order to be used in the track reconstruction analysis. Figure 16 shows, for one of the PMTs, the slewing and arrival time resolution parameterised as a function of the pulse height.

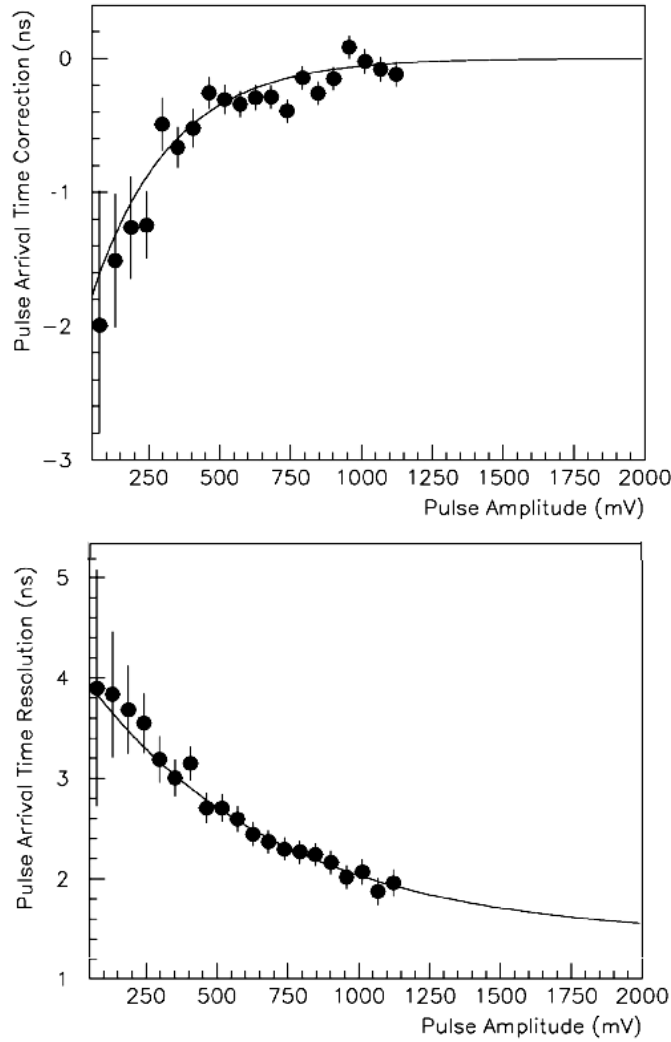


Figure 16: Measurement of the pulse amplitude dependence of the bias (slewing) and the resolution in evaluating the pulse arrival time, using the collected calibration data during operation.

7. Measurement of the zenith angle distribution of atmospheric muons.

From the total data sample collected with a 4-fold or higher coincidence trigger and 30mV PMT threshold, a subset containing 45800 events has been selected that have six or more PMT pulses (hits) within the 60 ns time window. These events have been analysed in order to reconstruct muon tracks. The arrival time of the digitized PMT pulses was used to estimate the muon track parameters by means of a χ^2 fit whilst the PMT pulse heights were used to reject ghost solutions and poorly reconstructed tracks. The details of the reconstruction strategy and the relevant studies are reported in another paper [29]. The results are summarized here.

From the selected sample of events, 745 muon tracks have been reconstructed that have a perpendicular distance from the center of the detector (impact parameter) greater than 6m.

Figure 17 shows the distribution of the azimuth angle of the reconstructed tracks. As expected, the distribution in azimuth of the muon tracks at the detector depth is not affected by the detector response or the reconstruction efficiency.

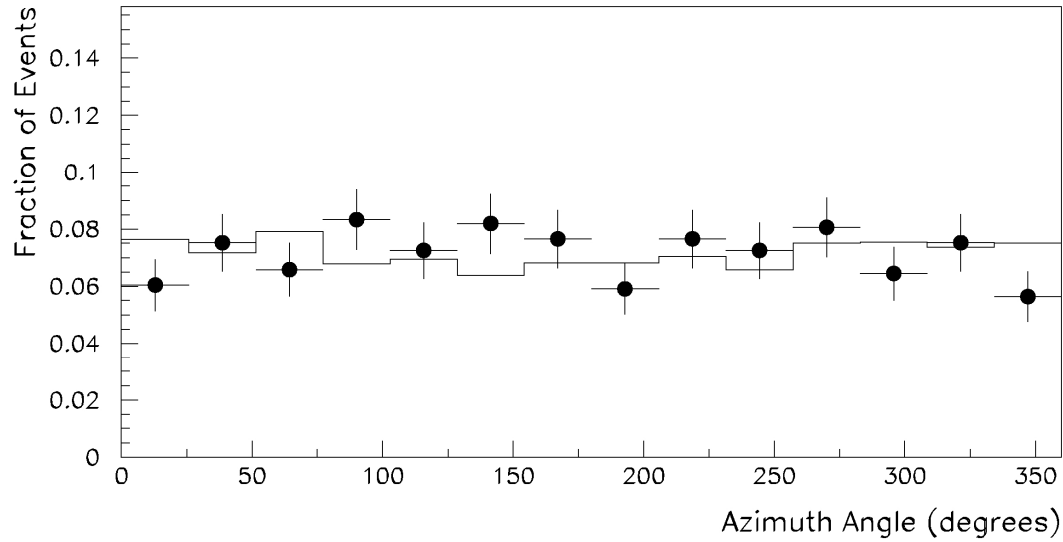


Figure 17: The experimental distribution of the reconstructed azimuth angles (solid points) compared with the Monte Carlo prediction (histogram).

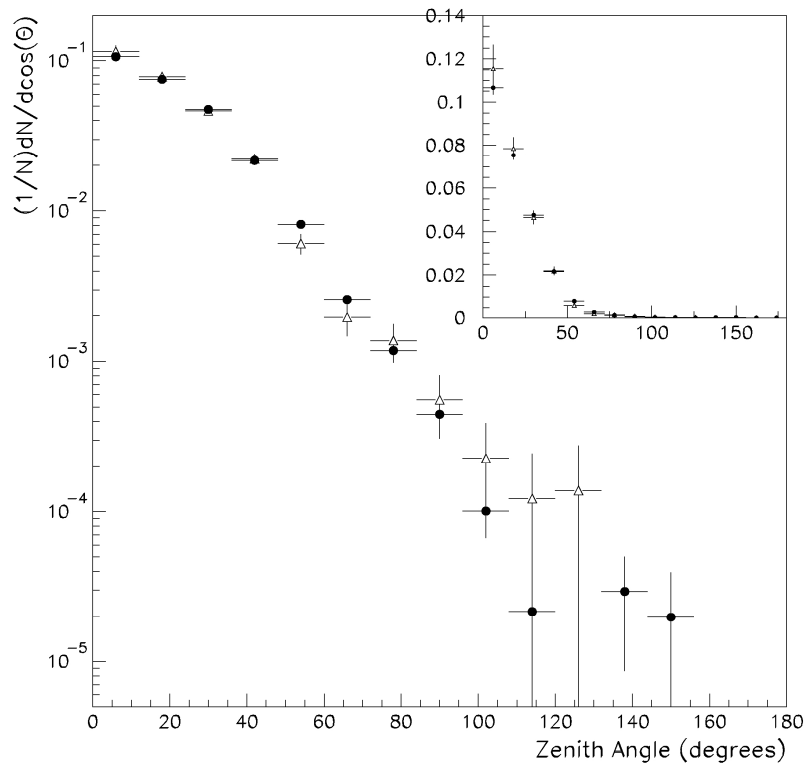


Figure 18: Zenith angular distribution (θ) of reconstructed tracks for the data (triangles) and Monte Carlo (solid points) event sample. The insert plot shows the same distributions on a linear scale.

The zenith angular distribution of the reconstructed tracks is compared to the Monte Carlo prediction in Figure 18. Due to the limited reconstruction resolution⁹, the distributions extend to zenith angles higher than 90°.

In order to quantify the level of agreement between the measured data and the predictions of the Okada model, the χ^2 probability (statistical similarity) of the experimental points to the Monte Carlo prediction was calculated. This was found to be 52%, demonstrating a very good agreement.

The number of atmospheric muons (N) arriving at the detector depth per unit solid angle (Ω), per unit time (t) and per unit area (S), $\frac{dN}{d\Omega \cdot dt \cdot dS}$, is usually parameterized as [15, 30-32]:

$$\frac{dN}{d\Omega \cdot dt \cdot dS} = I_0 \cdot \cos^\alpha(\theta) \quad (1)$$

where I_0 is the vertical intensity.

The index α has been found to be equal to 4.5 ± 0.8 in previous measurements at 3697m water depth at the Nestor site [15, 31]. The vertical intensity was evaluated by integrating equation (1) and setting the total number of muons equal to the total number of the reconstructed data tracks ($D=745$) divided by the total efficiency (ϵ) in reconstructing atmospheric muon tracks.

$$I_0 = \frac{\frac{D}{\langle \epsilon \rangle} \cdot (\alpha + 1)}{2 \cdot \pi \cdot T \cdot S} \quad (2)$$

where T stands for the total experimental time of 609580 s during which this data subset was accumulated.

The total efficiency (ϵ) has been estimated from the Monte Carlo simulated data as the ratio of the number of reconstructed tracks to the corresponding number of atmospheric muons generated with energies greater than 1 GeV at the detector depth (in a circle of 100 m¹⁰ radius at 100m above the detector). The total efficiency, corresponding¹¹ to a Monte Carlo production model following the angular distribution of equation (1), with $\alpha=4.5$, found to be: $\epsilon = 3.89 \cdot 10^{-4} \pm 0.04 \cdot 10^{-4}$.

The vertical atmospheric muon intensity, found using the formula (2) gives:

$$I_0 = 8.8 \cdot 10^{-9} \pm 1.3 \cdot 10^{-9} \text{ cm}^{-2} \cdot \text{s}^{-1} \cdot \text{sr}^{-1} \quad (3)$$

where the estimated error is calculated from statistical uncertainties in the data and Monte Carlo simulation and the measurement error on the index σ .

This is in good agreement with predictions of the vertical intensity of the atmospheric muons at a depth of 3800m.w.e, by Okada [27] ($I_0 = 8.8 \cdot 10^{-9} \text{ cm}^{-2} \cdot \text{s}^{-1} \cdot \text{sr}^{-1}$) and Bugaev et al ($I_0 = 9.0 \cdot 10^{-9} \text{ cm}^{-2} \cdot \text{s}^{-1} \cdot \text{sr}^{-1}$) [33, 34] as well as with the previous NESTOR

⁹ Monte Carlo studies [29] show an average reconstruction resolution of 11°.

¹⁰ Approximately twice the light transmission length in the water at the experimental site.

¹¹ The re-weighting of the Monte Carlo events, produced with the Okada model, to follow the differential flux of equation (1), is described in [29].

measurements [35] of $I_0 = 9.8 \cdot 10^{-9} \pm 4.0 \cdot 10^{-9} \text{ cm}^{-2} \cdot \text{s}^{-1} \cdot \text{sr}^{-1}$ at depths between 3700 and 3900m. It is also consistent with the DUMAND measurement [32] of $I_0 = 1.31 \cdot 10^{-8} \pm 0.4 \cdot 10^{-8} \text{ cm}^{-2} \cdot \text{s}^{-1} \cdot \text{sr}^{-1}$ at a depth of 3707m.

A more accurate analysis of the data with a simultaneous estimation of the index α and the vertical muon intensity I_0 is in publication. [29].

8. Conclusions

In March 2003, the NESTOR collaboration successfully deployed a test floor of the detector tower, fully equipped with final electronics and associated environmental sensors to a depth of 3800m, situated 80 meters above the sea bottom station.

The deployed detector was continuously operated for more than one month. The monitored experimental parameters, operational and environmental, remained stable within the accepted tolerances whilst the readout and DAQ chain performed well and with practically zero dead-time.

The 1.1% of the total experimental time was lost due to bioluminescent activity around the detector. Events collected during such periods of activity were easily identified and rejected.

Several studies have been made to ensure that the event selection trigger was unbiased and that the collected light on the PMTs can be attributed to the expected natural sources. The PMT pulse height distributions, the trigger rates and the total number of photoelectrons inside the trigger window as functions of the signal thresholds and coincidence level settings as well as the arrival time distribution of the accumulated photoelectrons, agree very well with Monte Carlo predictions based on the atmospheric muon flux parameterization of [27], on the natural K^{40} radioactivity in the sea water and the PMT dark currents and after pulses.

In parallel, calibration in the sea using the LED flasher units mounted above and below the detector floor, provided a rigorous test on the time stability of the detector as well as a measurement of the resolution of the arrival time of the PMT signals.

A subset of the accumulated data, consisting of events with six or more PMT pulses inside a 60ns time window, has been analysed and the trajectories of atmospheric muons have been reconstructed. The distributions of the azimuth and zenith angles of the reconstructed muon tracks are found to be in a very good agreement with Monte Carlo predictions, based on the atmospheric muon model of [27].

Finally, based on previous measurements by the NESTOR collaboration concerning the shape of the zenith angle distribution, we estimated the vertical atmospheric muon intensity at the deep-sea site. Our measurement, of

$$I_0 = 8.8 \cdot 10^{-9} \pm 1.3 \cdot 10^{-9} \text{ cm}^{-2} \cdot \text{s}^{-1} \cdot \text{sr}^{-1}$$

is in very good agreement with previous underwater measurements and with phenomenological expectations. A more detailed description of our data analysis and track reconstruction has been published elsewhere [29].

The objectives for this deployment of the NESTOR test detector were to perform a thorough test of the electrical supply and distribution systems, the monitoring and control

systems and the full data acquisition and transmission chain from the sea to the shore station. These objectives have been met successfully. In addition we have been able to demonstrate the ability of the proposed neutrino telescope to reconstruct muon trajectories.

Acknowledgements

The authors wish to acknowledge the help and support of all the members of the NESTOR collaboration. Our very sincere thanks are also due to the technical and support staff from the collaborating institutes, especially of the NESTOR Institute in Pylos and the “Institut für Angewandte Physik”, University of Kiel, for their unstinting efforts over several years. It is also a pleasure to acknowledge our many industrial partners for their essential contributions; in particular we express our gratitude to OTE S.A, the Greek Telecom Company for the substantial material support and for the sea and underwater operations that underpin the results presented here. Many thanks are due to the Masters, Crews and Cable Engineers on the THALES (OTE) and RAYMOND CROZE (France Telecom marine) and TENEO (Tyco) as well as the support vessel DYNATOS, for their help and advice in sea operations and deployments.

Last but not least, we greatly appreciate the support of many institutes and agencies that have provided funding for the NESTOR project; in particular the General Secretariat for Research and Technology of the Greek Ministry of Development, the General Secretariat of Peloponnesus and the German Bundesministerium für Bildung und Forschung, Germany. We are also grateful to the Wolfermann-Naegeli foundation in Kuesnacht (CH) for its support in the preparation phase leading to the results discussed in this paper. We hope that the completion of this important stage in this project demonstrates that their confidence was not misplaced.

References

- [1] DUMAND Proposal, Report No. HDC-3-88, 1988 (unpublished).
- [2] Balkanov V. A. et al [Baikal Collaboration], Nucl.Phys.Proc.Suppl. 87, pp 405-407 (2000).
- [3] Andres E. et al, Astropart.Phys. 13, 1-20 (2000).
- [4] Ahrens J. et al [Icecube Collaboration], Nucl.Phys.Proc.Suppl 118:388-395 (2003).
- [5] NESTOR: Proceedings of the 2nd NESTOR International Workshop, L. K. Resvanis editor (1992); Proceedings of the 3rd NESTOR International Workshop, L. K. Resvanis editor (1993); website <http://www.nestor.org.gr>.
- [6] ANTARES: Aslanides E. et al [ANTARES Collaboration], ANTARES Proposal, astro-ph/9907432 (1999); website <http://antares.in2p2.fr>.
- [7] NEMO: Migneco E. et al [NEMO Collaboration], “The NEMO Project”, Proceedings of the VLVnT Workshop pp 5-10, NIKHEF, Amsterdam 5-8 October 2003; website <http://nemoweb.lns.infn.it>.
- [8] Ball A. E. et al [NESTOR Collaboration], CERN Courier 43N9:23-25, 2003.
- [9] Peter K. F. Grieder [NESTOR Collaboration], Proceedings of the 28th International Cosmic Ray Conference (ICRC 2003).
- [10] Tsirigotis A. G [NESTOR Collaboration], Proceedings of the International Europhysics Conference on High Energy Physics (EPS 2003, Aachen Germany), The European Physics Journal C, ISSN:1434-6044.
- [11] Tzamarias S. E. [NESTOR Collaboration], Proceedings of the VLVnT Workshop pp 11-16, NIKHEF, Amsterdam 5-8 October 2003.
- [12] Resvanis L. K., Proceedings of the 8th International Workshop on Topics in Astroparticle and Underground Physics (TAUP 2003) September 5 - 9, 2003, University of Washington, Seattle, Washington.
- [13] Anassontzis E. G. et al, Sea Technology 44-10, 2003.
- [14] L. K. Resvanis, Proceedings of the 2nd NESTOR International Workshop, pp 1-19, L. K. Resvanis editor (1992).
- [15] L. K. Resvanis et al, “NESTOR: A Neutrino Particle Astrophysics Underwater Laboratory for the Mediterranean”, Proceedings of the High Energy Neutrino Astrophysics Workshop, V. J. Stenger, J. G. Learned, S. Paksava and X. Tata editors Hawaii (1992).
- [16] S. A. Khanaev et al, Proceedings of the 2nd NESTOR International Workshop, page 253, L. K. Resvanis editor (1992).
- [17] E. G. Anassontzis et al, Nuclear Instruments and Methods A349:242-246 (1994).
- [18] T. A. Demidova et al, Proceedings of the 2nd NESTOR International Workshop, page 284, L. K. Resvanis editor (1992).
- [19] E. Trimonis et al, Proceedings of the 2nd NESTOR International Workshop, page 321, L. K. Resvanis editor (1992).

- [20] E. G. Anassontzis, et al, Nuclear Instruments and Methods A479, pp 439-455 (2002).
- [21] M. Barone, Proceedings of 5th International Conference on Advanced Technology and Particle Physics (COMO 96), Como, Italy, 7-11 Oct 1996, Published in Nucl.Phys.Proc.Suppl.61B:159-163,1998.
- [22] P. Arragain, “NESTOR DAQ System on Shore”, LBNL (October 1999).
- [23] Joshua Sopher, “NESTOR FLOOR BOARD”, Technical Report, Internal NESTOR Publication 2002.
- [24] D. Nygren, et al, “NESTOR Data Acquisition System – Based on Waveform Capture”, August 20, LBNL (1998).
- [25] Stuart Kleinfelder, “Analog Transient Waveform Digitizer”, LBNL 1998.
- [26] S. Agostinelli et al, “GEANT4: A Simulation Toolkit”, Nucl.Instrum.Meth. A506:250-303, 2003.
- [27] A. Okada, Astroparticle Physics 2, 393 (1994).
- [28] E. J. V. Battle et al, Proceedings of the VLVnT Workshop pp 41-43, NIKHEF, Amsterdam 5-8 October 2003.
- [29] NESTOR Collaboration, “A measurement of the cosmic muon flux with a module of the NESTOR neutrino telescope”, to be published (2004).
- [30] Peter K. F. Grieder, “Cosmic Rays at Earth”, Elsevier, Amsterdam (2001), Chapter 4.
- [31] L. K. Resvanis, Proceedings of the 2nd NESTOR International Workshop, pp 1-19, L. K. Resvanis editor (1992).
- [32] J. Babson et al, Physical Review D42, 3613 (1990).
- [33] Edgar V. Bugaev, et al, Proceedings of the 3rd NESTOR International Workshop, page 268, L. K. Resvanis editor (1993).
- [34] Edgar V. Bugaev, et al, Physics Review D58, 054001 (1998).
- [35] I. F. Barinov et al, Proceedings of the 2nd NESTOR International Workshop, page 340, L. K. Resvanis editor (1992).